

Double nucleus in M83

Damián Mast¹, Rubén J. Díaz^{1,2}, M.Paz Agüero¹

damian@mail.oac.uncor.edu

Received _____; accepted _____

¹SeCyT, Universidad Nacional de Córdoba, Argentina

²Observatorio Astronómico de Córdoba, UNC, Laprida 854, 5000 Córdoba, Argentina

ABSTRACT

M 83 is one of the nearest galaxies with an enhanced nuclear star formation and it presents one of the best opportunities to study the kinematics and physical properties of a circumnuclear starburst. Our 3D spectroscopy data in R band confirm the presence of a secondary nucleus or mass concentration (previously suggested by Thatte et al. 2000). We determine the position of this hidden nucleus, which would be more massive than the visible one, and was not detected in the optical HST images due, probably, to the strong dust extinction. The optical nucleus has a mass of $5 \times 10^6 M_{\odot} / \sin i$ ($r < 1''.5$), and the hidden nucleus, located $3''.9 \pm 0''.5$ at the NW ($\text{PA } 271^\circ \pm 15^\circ$) of the optical nucleus, would have a mass of $1 \times 10^7 M_{\odot} / \sin i$ ($r < 1''.5$). The emission line ratio map also unveils the presence of a second circumnuclear ring structure, previously known by IR imaging (Elmegreen et al. 1998). The data allow us to resolve the behavior of the interstellar medium inside the circumnuclear ring and around the binary mass concentration.

Subject headings: galaxies: kinematics and dynamics, nuclei, starburst, structure — individual (NGC 5236) — techniques: spectroscopic

1. INTRODUCTION

M 83 is a very special case of nearby grand design barred spiral galaxy (Table 1), it harbors a nuclear X-ray source (Soria et al. 2002), coexisting with a massive starburst in a double circumnuclear ring (Elmegreen et al. 1998) and a secondary mass concentration recently suggested by Thatte et al. (2000) and confirmed by 3D spectroscopic data (Mast et al. 2002). Gallais et al. (1991) obtained infrared (IR) images of the central $20''$ in

the J , H and K bands and analysed the colour-colour diagrams which indicate that the nucleus and several regions in an arc at $7''$ from the nucleus are forming stars at a high rate. HST observations (optical and UV) and IUE spectra reveal that the arc contains more than 20 massive young clusters similar to 30 Dor in the LMC (Heap 1994), with ages between 2 and 8 million years and masses in the range $1 \times 10^4 - 1 \times 10^6 M_{\odot}$.

Thatte et al. (2000) made IR spectroscopic observations with two long slit positions of the nuclear region using the ISAAC spectrometer at the VLT. They detected two peaks in the radial velocity dispersion profile, one on the K -band luminosity peak, and the other one displaced about $3''$ to the SW, suggesting the presence of a secondary nucleus. The lack of two spatial dimensions in the spectroscopic information did not allow them to fix the precise position of the second mass concentration. Although the morphology of the star formation activity has been studied in detail (Gallais et al. 1991; Harris et al. 2001), there are very few kinematic or dynamical studies based in good spatial samplings. In this work we present a study of the 2D kinematics of the central region of this galaxy, which resolves the behavior of the interstellar medium around the binary mass concentration.

2. OBSERVATIONS

A summary of the observations is presented in Table 2. We made three-dimensional (3D) spectroscopic observations of the central region of M 83 using the Multifunctional Integral Field Spectrograph mounted on the 1.54 m telescope at Bosque Alegre Astrophysical Station (Díaz et al. 1999, 2003). The data were gathered between March 2001 and May 2002.

The analysed integral field was obtained with a total exposure time of 2 hours. The spectra, with a resolution of 1.5 \AA in the R band, were obtained with an array of 8×14

lenses ($1''.5$ field each one) sampling a field of $12'' \times 21''$. The seeing was about $2''$ so the field is slightly subsampled. We complemented these data with archival HST images in the filters F187N, F190N (Pa α and Pa α continuum), F814W (7940 Å) and F656N (6563 Å).

3. DATA REDUCTION AND ANALYSIS

The reduction of the spectra was performed with the software SAO (developed by the Special Astrophysical Observatory, Russia), the software ADHOC (Boulesteix 1993) and PC standard worksheets. The procedure followed is described in detail in the works of Díaz et al. (1997), Vega (2000) and Mast (2000). The spectra include the nebular emission lines H α , [NII] 6548 Å, 6583 Å, [SII] 6716 Å and 6731 Å which were fitted using gaussian curves to determine the parameters that describe them. In most of the field, the S/N allowed the detection and fitting of the mentioned emission lines, but in some locations (in the field SW border) the S/N ratio of the spectrum was low and only H α and [NII] 6583 Å emission were detected. We made gaussian fitting up to a level of 20% of the peak value. Therein the profile tails that in some locations could appear do not affect strongly the manual interactive fitting performed to the lines. Once the emission line gaussian fitting was completed, we obtained the following data for each lens: H α , [NII] 6583 Å, [SII] 6717 Å and [SII] 6731 Å fluxes, wavelength positions and FWHM of each line. With this information the following maps were constructed: Red continuum intensity, H α intensity, [NII] 6583/H α , ([SII] 6717+[SII] 6731)/H α , [SII] 6717/[SII] 6731, and FWHM maps. Because the H α line is the most conspicuous emission of the obtained spectra and the one showing better S/N ratio, we only analysed the radial velocities corresponding to this line. A map of the radial velocity field was also constructed.

As mentioned before, the field was slightly subsampled. In order to improve the data processing and visualization, all the field values were interpolated, yielding the same

field sampled by 24×42 elements ($0.5''/\text{pixel}$). The internal error due to the velocity determination procedure has a relative value lower than 5 km sec^{-1} (r.m.s.). That is the precision limit in the velocity field determination, in case we have data with good S/N ratio (> 10). In our case the best S/N ratio in the $\text{H}\alpha$ emission line is $S_{Total}/N = 30$, $S_{Peak}/N = 15$; the worst S/N , in one of the outermost lenses, is $S_{Peak}/N = 2$.

4. RESULTS

4.1. Morphological scenario

Figure 1 shows the central $40'' \times 40''$ around the optical nucleus from which a bright small red arc emerges to the SW, but the most conspicuous feature is a giant star forming arc (Gallais et al. 1991; Elmegreen et al. 1998). In this one, to the NE of the nucleus several star clusters are present and have been studied by Harris et al. (2001). Going counterclockwise through the arc, a highly obscured region is located with a large number of dust patches and a star forming region emerging from the dust, more than $5''$ westward from the nucleus. The R band continuum map (Fig. 2) shows an ellipsoidal light distribution with the external isophotes center located $3''$ to the W-SW of the continuum emission peak, which we assumed, corresponds to the optical nucleus position. This result is consistent with the observations of Thatte et al. (2000), who found that the nucleus is not located at the symmetry center (of the circumnuclear light distribution) in their K band images. Assuming that the symmetry center (outer isophotes) is the same for R and K bands, the nucleus would not be exactly located at the bulge center. (See the sketch in Fig. 3).

4.2. Radial Velocity Field of the Ionized Gas

Figure 4 shows the obtained velocity field, which covers $12'' \times 21''$ of the central region of M 83. A square marks the position of the optical nucleus, which corresponds to the continuum image peak (at R band, N_R in Fig. 3 and 4). The isovelocity lines were traced each 10 km sec^{-1} (2σ uncertainty). The isovelocity lines are strongly distorted and could indicate a departure from the axisymmetric potential, with a main line crowding at the position indicated by a circle, where the hidden nucleus should be located. The radial velocity field has a distortion that indicates the presence of two mass concentrations, neither of them located exactly on the global velocity field minor axis (dotted line in Fig. 4 and 6).

The radial velocity field is similar to that of the central region of NGC 3227 (Arribas & Mediavilla 1994), which shows an AGN out of the kinematic center of the galaxy.

The extreme velocity values of the observed field are $V_{max} = 634 \text{ km sec}^{-1}$ and $V_{min} = 542 \text{ km sec}^{-1}$ ($\Delta V = 92 \text{ km sec}^{-1}$).

There is an isovelocity line stretching (Fig. 4b) which is coincident, within the uncertainties, with the continuum peak previously identified with the optical nucleus, and therefore is about $3''$ to the N-NE of the red continuum symmetry center (C_R in Fig. 3 and 4).

The radial velocity gradient determined by the line stretching indicates that the mass concentration of the hidden nucleus would be larger than that of the visible one.

Areas with predominant circular motion can be drawn around each mass concentration (see Fig. 5). Each area involves 6 lenses (optical nucleus) and 11 lenses (hidden nucleus).

The mass concentration corresponding to the optical nucleus and, within the uncertainties, coincident with the continuum peak position, is at $2''.3 \pm 0''.5$ to the W-SW from the red continuum symmetry center, while the hidden nucleus, kinematically

determined, would be at $2''.4 \pm 0''.5$ NW from the red continuum symmetry center. Therefore, the hidden mass concentration is $3''.9 \pm 0''.5$ at PA $271^\circ \pm 15^\circ$, from the optical nucleus (continuum emission peak). Using the astrometric parameters of the HST WFPC observations, we derive the position of the main nucleus: (J2000) $\alpha = 13h\ 37m\ 00.919s$, $\delta = -29^\circ 51' 55'' 66$ with a $0''.1$ uncertainty. Assuming that this is the position of the peak continuum emission in our maps, the coordinates of the hidden nucleus would be $\alpha = 13h\ 37m\ 00.540s \pm 0.04s$, $\delta = -29^\circ 51' 53'' 62 \pm 0''.5$, considering an uncertainty in the position of $1/3$ of sampling element. Is important to note that the main source of uncertainty in the nuclei positions is the astrometry. The hidden nucleus is at the NW extreme of the star formation arc. Its position can be projected on the long slit direction of Thatte et al. (2000) and it is seen that it is at the same position were this authors note a local maximum in the stars velocity dispersion. The main difference is $2''.5$ along a direction perpendicular to the slit of Thatte et al. (2000).

The observed region is too small on galactic scale, also perturbed and, in order to derive the kinematic parameters, therein we smoothed the observed radial velocity field with a median filter of size $6'' \times 6''$. The result is shown in Figure 6. The PA of the minor axis is 138° , very near to the PA of the low resolution CO velocity field determined by Lundgren et al. (2004) of 136° . Therefore we assumed for the masses estimations, an inclination equal to the global inclination value of 24° (Comte 1981). The estimated masses of the nuclei within a $1''.5$ radius would be around $1.2 \times 10^7 M_\odot$ (optical nucleus) and $2.4 \times 10^7 M_\odot$ (hidden nucleus). There is no intention to report strict Keplerian rotation around the mass concentrations, we just note a predominance of circular motions involving several detection elements (lenses) and we derive upper limits for the masses.

In order to see if the gas is in ordered rotation around the mass concentrations we studied the line profiles. A strongly asymmetric line profile, with pronounced wings on one

side is more likely due to non gravitational motions. As can be seen in Figure 7, this is not the case for the spectra in the hidden nucleus position.

4.3. FWHM map

Figure 5 shows a FWHM map with the radial velocity field superposed. Two local peaks coincident, within the uncertainties, with the position of the two mass concentrations indicated in Figure 4, can be seen. We note here that the lack of exact coincidence between kinematic centers and FWHM peaks, could be real. This is the case of M 31 double nucleus (See Fig. 7 of Bacon et al. 2001) where the lack of symmetry in the gravitational potential generates a difference in the locations of the rotation center and the observed velocity dispersion peaks at a given resolution. Therefore, the motion is circular only in an approximate approach that allows the mass estimations.

In the SW part of our FWHM map, profile widths exceed 200 km sec^{-1} . This could be due to shocks in the ionized gas considering that this region coincides with the star forming arc.

4.4. [NII] 6583 / H α map

Figure 8 shows the [NII] 6583 / H α ratio. The position of the optical nucleus is marked with a star. A ring of mean value 0.62 is appreciable around the optical nucleus, coincident with the inner ring reported by Elmegreen et al. 1998 (Fig. 8b). The ratio is comparatively low in the inner ring region (nuclear region) and in the star forming arc, ranging from values between 0.40 in the star forming arc to 0.46 in the inner ring region. Those values are the expected for HII regions (lower than 0.5, Osterbrock 1987). The peak value in the ring is $\sim 0.73 \pm 0.02$. Assuming that those ratios depend mainly on the abundance effects,

their distribution would indicate that the relative abundance of nitrogen is higher in the ring than in the nuclear region and the star forming arc. The low $I(\lambda 6584)$ in relation to $H\alpha$ suggest that the starburst in the nuclear region and in the star forming arc is younger than in the ring. The values at the region of $3''$ around the hidden nucleus are $\sim 0.66 \pm 0.02$.

5. DISCUSSION

It is important to note that the circular motion around both regions has been measured within several detection elements. Furthermore the local kinematics suggests that the secondary nucleus is more massive, but another possibility must be mentioned: a warp in the nuclear region could produce a strong change in the inclination of the orbits of the ionized gas clouds, e.g. Schinnerer et al. (2000). This strong distortion of the kinematic minor axis could eventually mimic a binary mass concentration but the shape of the observed velocity field would be very difficult to reproduce with a mild local change of geometrical parameters, as the case described by these authors. In order to yield much greater insight into the physics of the nuclear region, we use the $H\alpha$ and $Pa\alpha$ HST images (like the one produced by Harris et al (2001) for the $H\alpha/H\beta$ ratio), together with case B recombination theory, to construct an extinction map (Fig. 9). It can be seen that the strong extinction is very localized and would not play an important role in the kinematics.

The position of the hidden nucleus is within the uncertainties coincident with a knot appearing at K band. This could be the IR source corresponding to the hidden mass concentration. The $H\alpha$ map, not shown here, does not clearly reveal the existence of the innermost circumnuclear ring reported by Elmegreen et al. 1998. Frequently such rings are constituted by a discrete series of emission regions. In this case, the ring is conspicuous in the near IR colour maps presented by Elmegreen et al. 1998 and in our $NII/H\alpha$ map, probably suggesting different properties (mainly age) in the HII regions, instead of an

enhanced star formation outside this innermost ring. The most evident H α structure is a star forming arc that extends from the SE to the NW, which would be part of an outermost circumnuclear ring (Elmegreen et al. 1998).

One question arises here: if the velocity field distribution corresponds to a binary mass concentration, can the star formation be triggered by the passage of the hidden nucleus through the high gas density medium? If this would be the case, then the age gradient in the star forming arc (Gallais et al. 1991, see introduction) that ends in the hidden nucleus would provide the clue to the dynamical evolution of this complex system.

6. CONCLUSIONS

In this work we studied the morphology, the ionized gas emission and the kinematics in the innermost regions of M 83. The hidden nucleus is not evident in the HST images, although kinematically the radial velocity field points out the presence of a strong mass concentration that could be the mentioned nucleus.

[NII] emission is relatively lower compared with H α emission of the hidden nucleus region, at the younger end of the starforming arc. This would be consistent with lower metalicity values at this region, but the lack of more emission line ratios precludes a direct confirmation with the data presented here. Notwithstanding, two independent works confirmed through photometry (Harris et al. 2001) the age gradient of this star forming arc. The emission line ratio map also unveils the presence of a second circumnuclear ring structure, previously known by IR imaging (Elmegreen et al. 1998).

The optical nucleus would have a Keplerian mass of $5 \times 10^6 M_\odot / \sin i$ ($r < 1''.5$), and the secondary nucleus, located $3''.9$ at the NW (PA 271°) of the optical nucleus, would have mass of $1 \times 10^7 M_\odot / \sin i$ ($r < 1''.5$). The FWHM map presents local maximums in the nuclei

positions, supporting the conclusion about the presence of two central mass concentrations derived from the radial velocity map.

The behavior of the interstellar medium inside the circumnuclear ring and around the binary mass concentration has been resolved. The hidden nucleus is located on the younger end of the giant arc of star formation; suggesting that the local departure of an axisymmetric gravitational potential would be the trigger of the nuclear starburst in M 83.

7. Acknowledgements

We thank the generous support of Germán Gimeno and Walter Weidmann during the observations. This work was partially financed by a grant from Agencia Córdoba Ciencia.

REFERENCES

Arribas, S., Mediavilla, E., 1994, ApJ, 437, 149

Boulesteix, J. 1993, ADHOC Reference Manual, (Marseille: Pub. De l'Observatoire de Marseille)

Bacon, R., Emsellem, E., Combes, F., Copin, V., Monet, G., Martin, P., 2001, A&A, 371, 409

Comte, G., 1981, A&AS, 44, 1981

de Vaucouleurs, G., de Vaucouleurs, A., Corwin, H. Jr., Buta, R., Paturel, G. and Fouque, P., 1991, Third Reference Catalogue of Bright Galaxies, Springer, New York

Díaz, R., Dottori, H., Carranza, G., Goldes, G. 1999, ApJ, 512, 623

Díaz, R., Paolantonio, S., Goldes, G., Carranza, G. 1997, Multifunctional Integral Field Spectrograph, Astronomy Papers 1/97, Fa.M.A.F., National University of Cordoba, 120 pp.

Díaz, R., Dottori H., Vera-Villamizar N., Carranza G., ApJ, 597, 860

Elmegreen, D., Chromeley, F., Warren, A., 1998, AJ, 116, 2834

Gallais, P., Rouan, P., Lacombe, D., Tiphene, D., Vauglin, L., 1991, A&A, 243, 309

Genzel, R., Weitzel, L., Tacconi-Garman, et al. 1995, ApJ, 444, 129

Harris, J., Calzetti, D., Gallagher, J., Conselice, C., Smith, D., 2001, AJ, 122, 3046

Heap, S., 1994, in Violent Star Formation: from 30 Dor to QSOs, Ed. G. Tenorio Tagle (Cambridge University Press), 303

Lundgren, A., Olofsson, H., Wiklind, T., Rydbeck, G., 2004, A&A, 422, 865L

Mast, D., Díaz, R., Agero, M.P., Weidmann, W., Gimeno, G., 2002, Espectroscopía de Campo Integral de la Región Central de NGC 5236, BAAA No. 45

Mast D., 2002, Master level dissertation, National University of Crdoba. See abstract in Mast et al. 2002

Oddone M. A., Goldes G., Carranza G., Díaz R., Plana, Boulesteix, 1999, BAAA 43, 70

Osterbrock, D. E. 1987, Astrophysics of Gaseous Nebulae and Active Galactic Nuclei, University Science Books

Schinnerer, E., Eckart, A., Tacconi L.J., Genzel, R., Downess, D., 2000, ApJ, 533, 850

Soria, R., Wu, K., 2003, A&A, 410, 53

Thatte, N., Tecza, M., Genzel, R., 2000, A&A, 364, L47

Vega, L., Díaz, R. J., Lípari, S., Storchi-Bergmann, T., Dottori, H., 2000, Cinemática y Espectrofotometría de NGC 5248, No. 44 BAAA, p.68

Vega L., 2000, Master level dissertation, National University of Córdoba. See abstract in Vega et al. 2000

Table 1. M 83 Characteristics

Feature		Reference
M	-20.4	¹
D (h = 0.75)	3.7 Mpc	²
Size	12'.9 × 11'.5	^{1, 7}
B_T	8.20 mag	^{2, 7}
V_\odot	503 km sec ⁻¹	²
Kinematic major axis	PA 46°	⁶
i	24°	³
Inner CN ring radius	2.8'', 51 pc	⁴
Outer CN ring radius	8.6'', 152 pc	⁴
Bar length	354'', 6 kpc	⁵

¹Oddone 1999²de Vaucouleurs et al. 1991³Comte 1981⁴Elmegreen et al. 1998⁵DSS image⁶Lundgren et al. 2004⁷Measured at $\mu_B = 25 m_B$ arcsec⁻²

Table 2. Log of Observations

	Date	Exp.Time	λ_0	$\Delta\lambda$	PA	Pixel scale	Field of view	Comments
		[sec]	[Å]	[Å]	[deg]		[arcsec]	
HST	May 2000	600	6563	21	209°	0''.049	160'' \times 160''	H α image
HST	April 2000	160	7940	1531	209°	0''.049	160'' \times 160''	Red continuum image
HST	May 1999	160	18739	187	212°	0''.075	19''.2 \times 19''.2	Pa α image
BAlegre	May 2002	3600	6600	800	96°	1''.5, 0.78 Å	12'' \times 21''	Integral Field
BAlegre	May 2002	3600	6600	800	96°	1''.5, 0.78 Å	12'' \times 21''	Integral Field

Note. — BAlegre: Estación Astrofísica de Bosque Alegre.

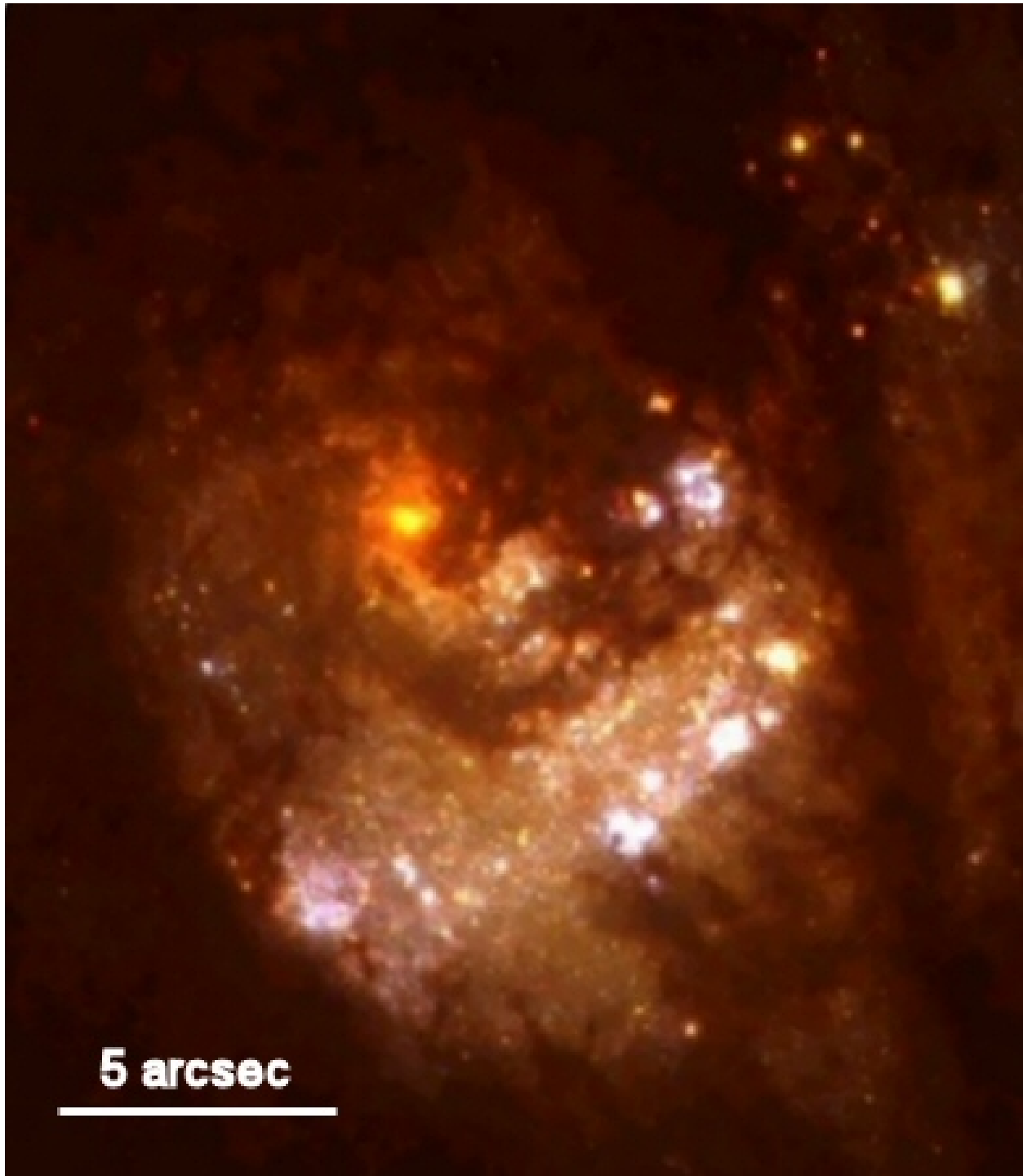


Fig. 1.— HST false colour image combined from B and (V+R) bands (F439W and F555W+F702W). North is at the top and east is at the left.

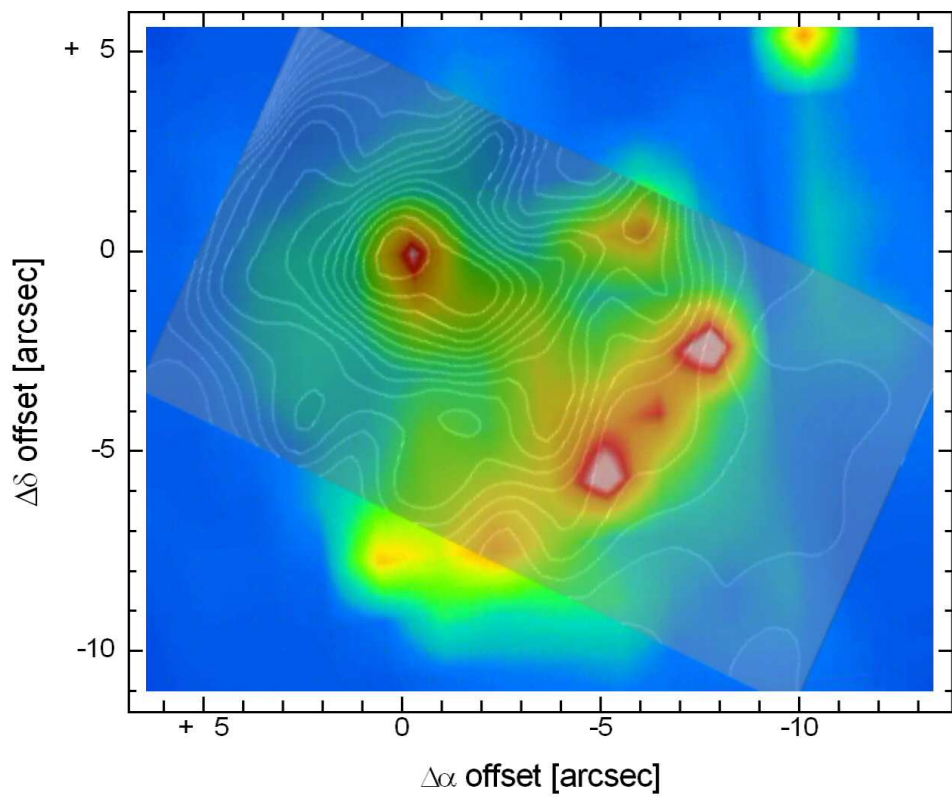


Fig. 2.— Map of red continuum relative intensity (isophotes) superposed to F814W HST image.

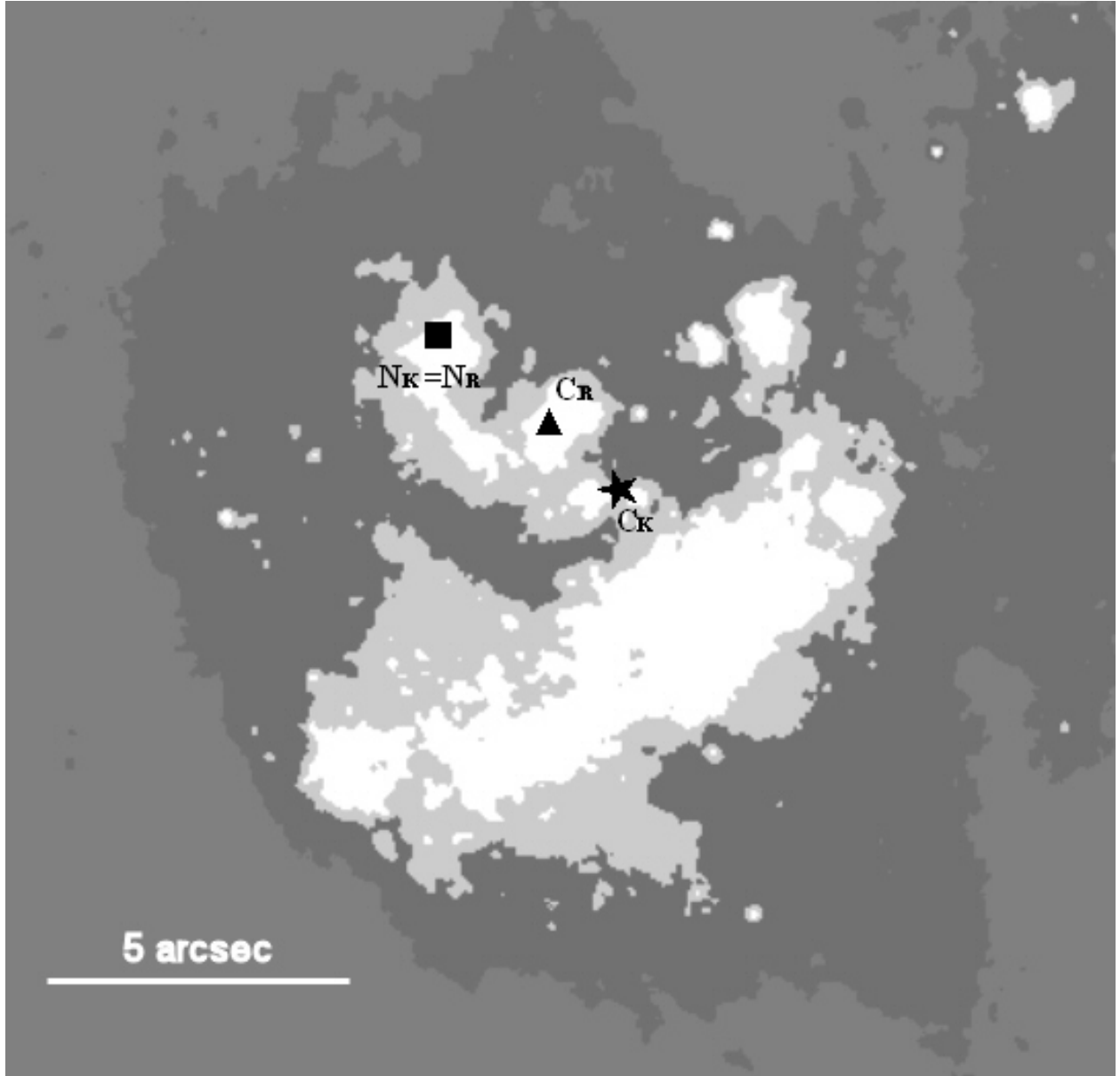


Fig. 3.— Sketch of NGC 5236 central region. North is at the top and east is at the left. A square marks the position of the optical nucleus, which corresponds to the continuum image peak (at R band, N_R). A triangle marks the position of the red continuum symmetry center (C_R). A star marks the position of the symmetry center of the outer isophotes in the K band image (C_K).

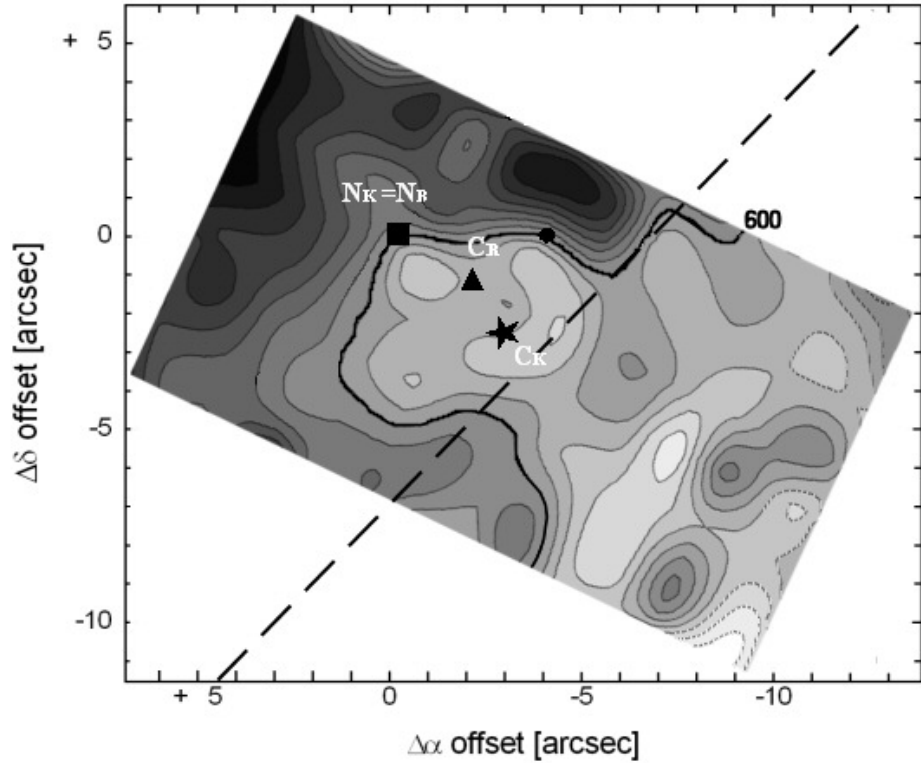


Fig. 4.— H α radial velocity field. A square indicates the position of the optical nucleus and a circle marks the position of the hidden mass concentration. The isovelocities are depicted each 10 km sec^{-1} (2σ uncertainty). The highest and lowest values are 634 km sec^{-1} and 542 km sec^{-1} , respectively. Dark is blueshift and light is redshift. A thicker contour corresponds to the systemic velocity. The dotted line marks the global minor axis at PA 136° . The isovelocity contours with less robust S/N values have been marked with dotted lines.

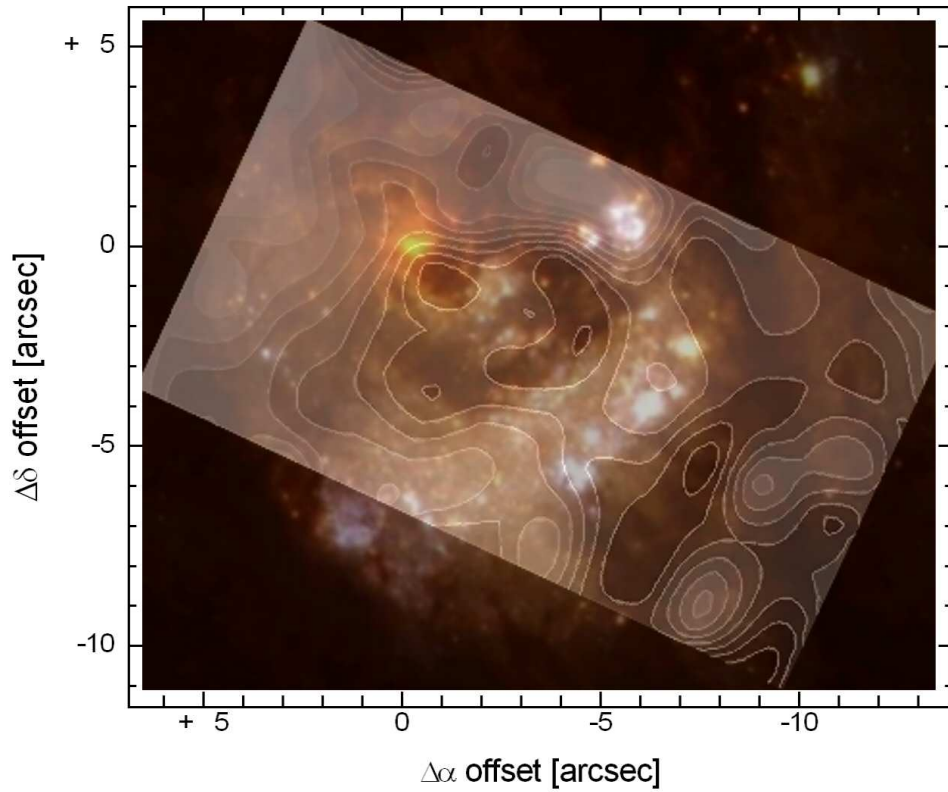


Fig. 4b.— H α radial velocity field + HST false colour image. Note the line stretching coincident with the continuum peak. North is at the top and east is at the left.

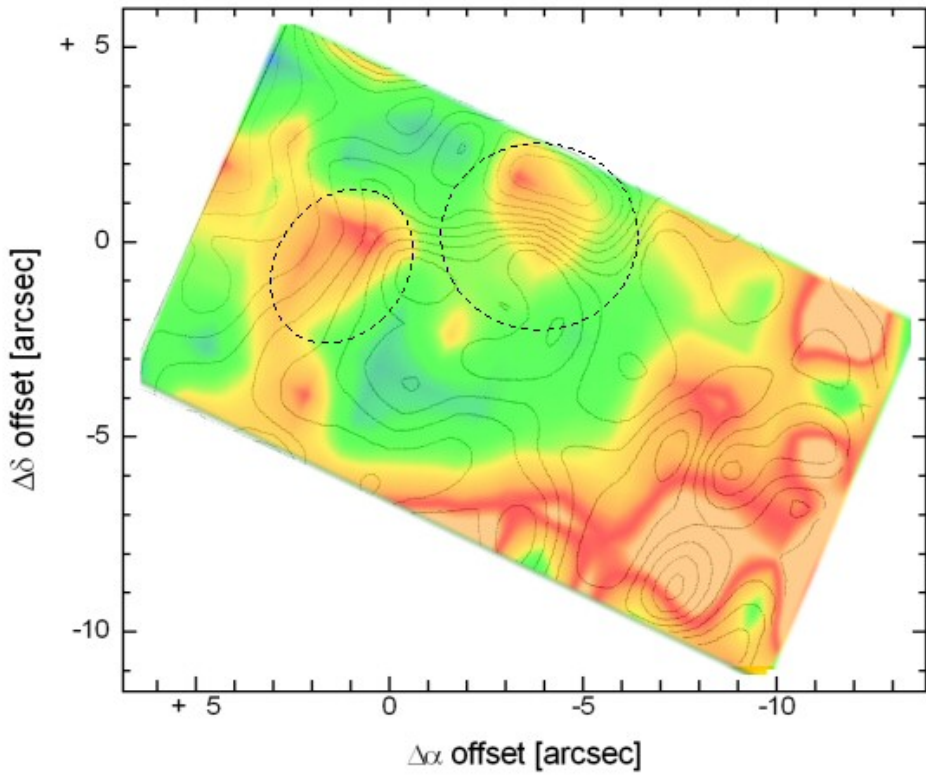


Fig. 5.— Distribution of radial velocity FWHM, the highest values are depicted dark. The isolines correspond to the H α velocity field. The darkest zones correspond to FWHM \sim 200 km sec $^{-1}$. Areas with predominant circular motion are drawn with dotted lines. In the darkest zones the line widths are not distinct from the instrumental profile.

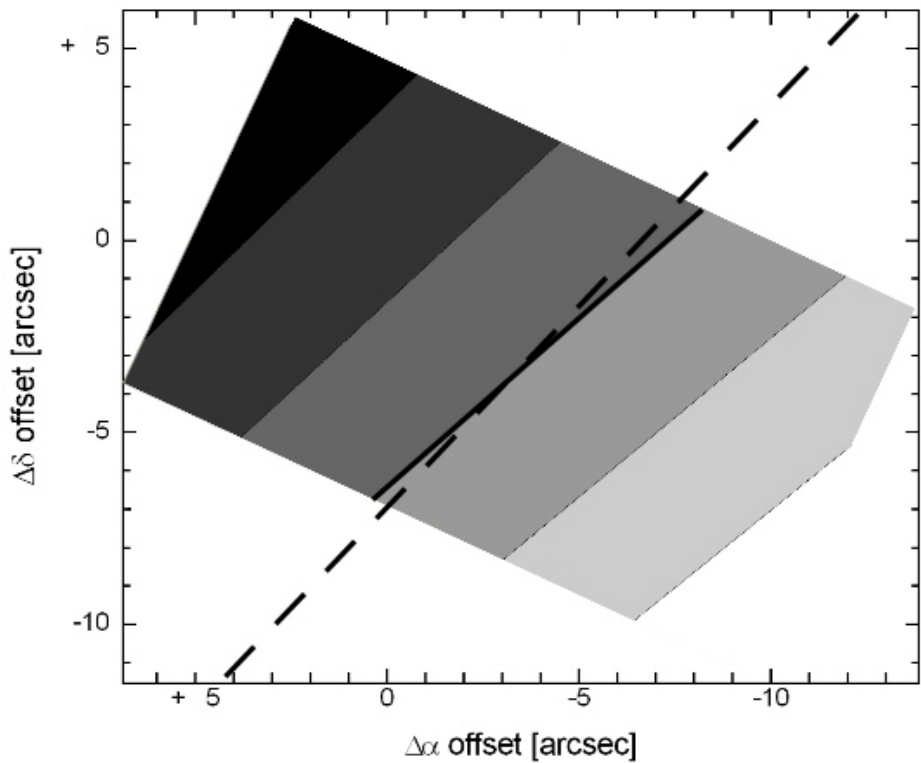


Fig. 6.— Smoothed radial velocity field. The minor axis PA of the resultant smoothed field is 132° . A thick contour marks the systemic velocity. Also drawn with a dotted line is the global CO velocity field minor axis PA of 136° (Lundgren et al. 2004).

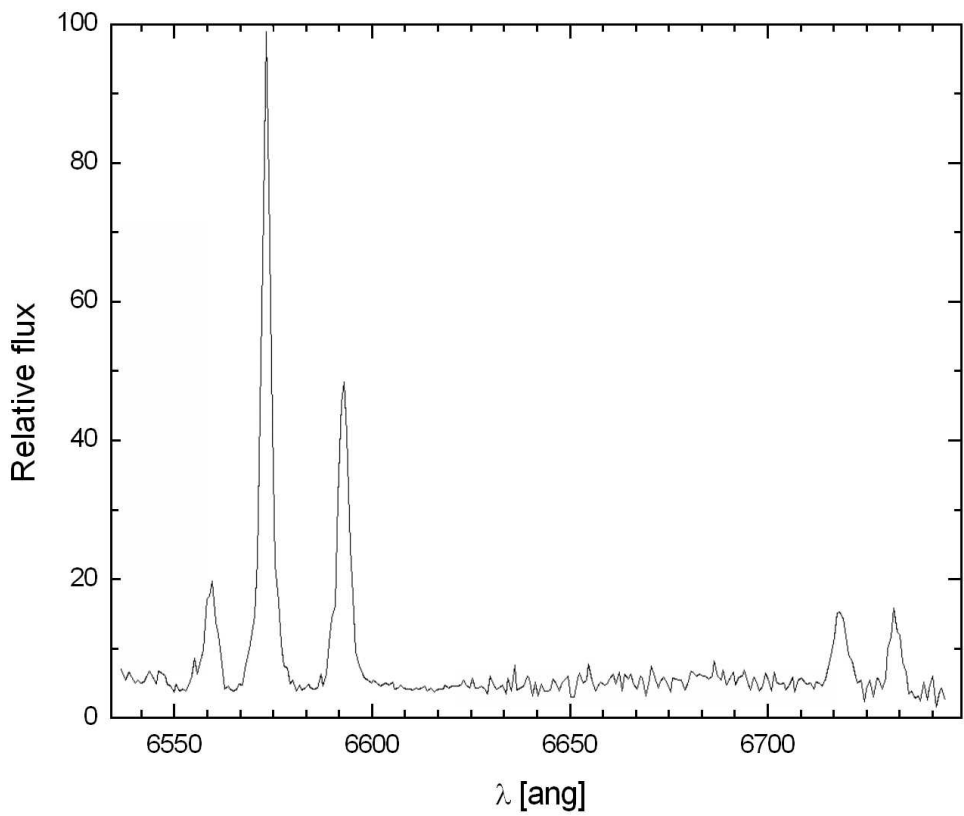


Fig. 7.— Spectra of the hidden mass concentration region. Note that there are not strong asymmetries in the line profiles.

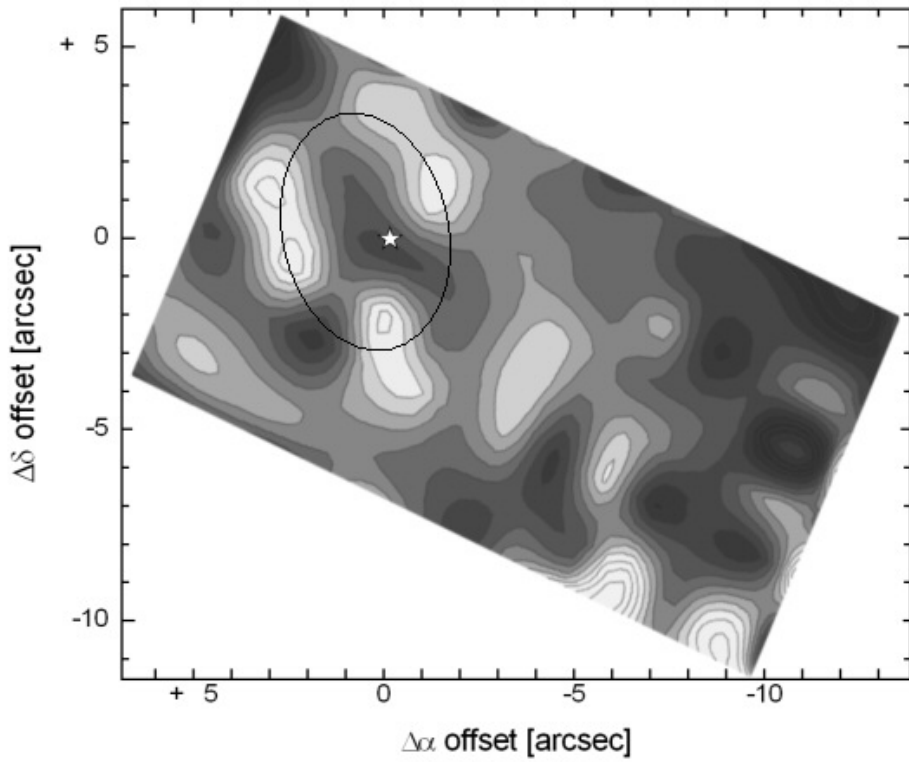


Fig. 8.— NII/H α ratio map. The peaks of NII/H α ratio > 0.6 (lightest in the figure) are surrounded by a dark contour.

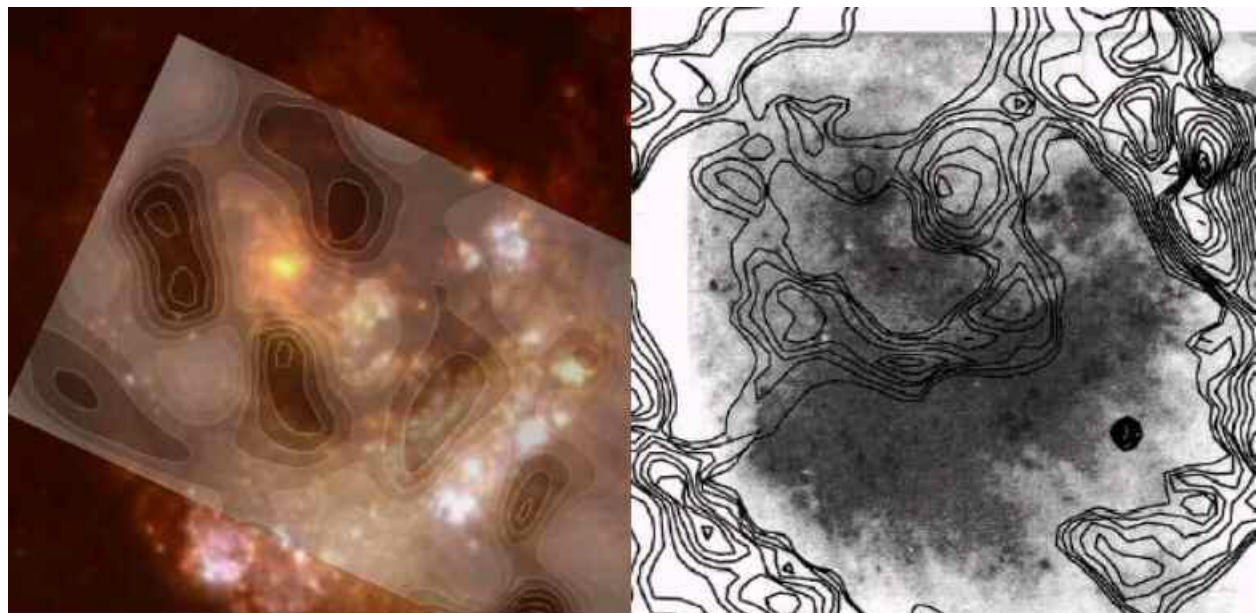


Fig. 8b.— *Left.* NII/H α ratio map superposed to the false colour HST image. *Right.* (J-K) unsharp-masked contours overlaid on an HST V-band image by Heap (1994) (Figure 5 from Elmegreen et al. 1998).

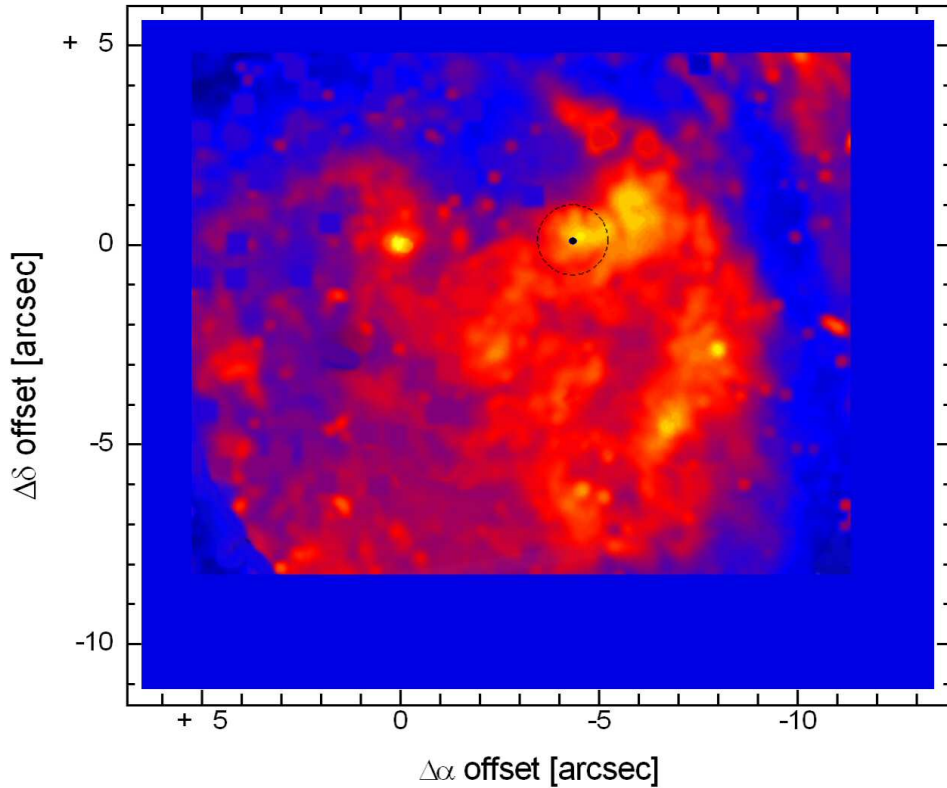


Fig. 9.— “Extinction” map generated from the $\text{Pa}\alpha/\text{H}\alpha$ HST images ratio. Pixel values range from 0.26 at the optical nucleus (yellow) to 1.8 at $(\Delta\alpha; \Delta\delta)=(-5''; 2''.5)$ (red). A dark circle marks the position of the hidden mass concentration and a dotted circle marks the uncertainty in the coordinates. Blue regions correspond to the dust lane, where signal in the narrowband images is lost because of heavy extinction.